

## Cracking in shotcrete tunnel shells

Roman Lackner & Herbert A.Mang

Institute for Strength of Materials, Vienna University of Technology, Vienna, Austria

**ABSTRACT:** In this paper, a material model for the numerical simulation of cracking of shotcrete is presented. Cracking is described by means of a multi-surface chemoplasticity model formulated in the framework of thermodynamics of chemical reactive porous media. The material model is calibrated by means of the fracture energy concept. This concept is extended towards chemoplasticity accounting for early-age cracking of shotcrete and towards consideration of interaction between shotcrete and the reinforcement. The applicability of the material model is demonstrated by means of a numerical analysis of a shotcrete tunnel shell of the Sieberg tunnel, Lower Austria. For this purpose, a hybrid method proposed by (Rokahr & Zachow 1997) is reformulated. The term “hybrid” refers to the combination of *in situ* displacement measurements and a material model for shotcrete. The amount of cracking in the shotcrete shell is investigated. From the obtained stress state, a “level of loading” is computed serving as safety measure of the shell.

### 1 INTRODUCTION

If high flexibility is required during tunnel excavation (e.g. in difficult ground conditions and/or in urban areas), the New Austrian Tunneling Method (NATM) has proved to be a powerful mode of construction. Having been applied world-wide since the 1950's, its success strongly depends on the experience of engineers. However, the demand for assessment and specification of the load-carrying behavior of tunnels, which allows an improvement of tunneling with respect to economy and safety, continues to increase. E.g., *in situ* measurements of displacements by means of a monitoring system are standardly used nowadays in NATM tunneling. They deliver 3D displacement vectors at points of the tunnel shell which are arranged in a relatively dense grid. Recently, hybrid methods combining these measurements with a constitutive law for shotcrete were developed (Rokahr & Zachow 1997) (Hellmich et al. 1999). They allow the quantification of stress states in shotcrete shells<sup>1</sup>. The employed material model for shotcrete has to account for chemical, thermal, and mechanical cross-effects, see (Hellmich et al. 1999). Such thermochemomechanical material models are formulated in the framework of thermodynamics of chemical reactive porous media (Coussy 1995). Recently, the ma-

terial model proposed in (Hellmich et al. 1999) was extended towards consideration of creep as reported in (Sercombe et al. 2000) and towards modeling of brittle failure (Lackner et al. 2001), finally accounting for

- increasing stiffness and strength in consequence of hydration,
- chemical shrinkage,
- creep, and
- microcracking.

Cracking of shotcrete is caused by bending moments in the shell induced by heterogenous soil and rock conditions. Moreover, shrinkage and thermal gradients (both in space and time) result in tensile loading favoring the development of cracks. In general, shotcrete shells are reinforced by means of two layers of reinforcement grids. As known from reinforced concrete design, the presence of reinforcement leads to a distribution of cracks finally resulting in a stabilized crack pattern (see, e.g. (Hofstetter & Mang 1995)).

In this paper, the material model developed by (Hellmich et al. 1999) and improved by (Sercombe et al. 2000) (Lackner et al. 2001) is extended towards consideration of early-age fracture of shotcrete. The maximum tensile stress (Rankine) criterion is used

<sup>1</sup>When tunnels are driven according to the NATM, shotcrete is applied onto the newly excavated cross-section forming a thin, flexible shell.

to control the tensile stresses in the shotcrete shell. The softening curves, which define the decrease of the tensile strength in consequence of microcracking, are calibrated by means of the fracture energy approach (Hillerborg et al. 1976). The interaction between shotcrete and the reinforcement bars, resulting in the so-called tension-stiffening effect, is considered within the calibration of these softening curves (Lackner 2000) (Lackner & Mang 2000).

The remainder of this paper is organized as follows: In Section 2, the hybrid method for the analysis of tunnel shells is described. A new structural model is proposed. Section 3 deals with the employed thermochemoplastic material model for shotcrete. For the calibration of the material model, the fracture energy approach is extended towards chemoplasticity allowing the simulation of early-age cracking. Finally, a hybrid analysis of the shotcrete tunnel shell at the Sieberg tunnel in Lower Austria is performed. The respective numerical results including the "level of loading" of the shell are presented in Section 4.

## 2 HYBRID METHOD FOR THE ANALYSIS OF SHOTCRETE SHELLS

In the context of tunnel shell analyses, hybrid methods are characterized by the combination of *in situ* displacement measurements with a material law for shotcrete. Displacements are monitored at measurement points (MPs). The MPs are arranged within measurement cross-sections (MCSs), see Figure 1. The distance between adjacent MCSs ranges from 5 to 10 m. In 1995, (Zachow 1995) proposed to compare *in situ* measured displacements with numerically obtained displacements. For this purpose, a large number of finite element (FE) analyses characterized by varying loading conditions was performed, providing sets of displacements together with corresponding stress states. Based on these sets, the actual stress state in the tunnel shell can be estimated by identifying the analysis which gave displacements similar to the ones measured on site (see, e.g. (Rokahr & Zachow 1997)). Figure 2 shows the employed structural model used

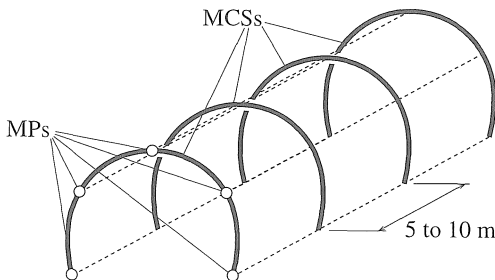


Figure 1: Illustration of the location of MPs installed at MCSs in tunnels driven according to the NATM

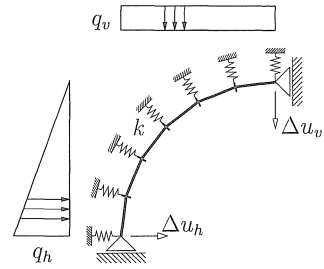


Figure 2: Hybrid method for the analysis of shotcrete shells: structural model proposed by (Zachow 1995)

by (Zachow 1995). Only a part of the shotcrete shell is considered. It is discretized by means of beam elements.

(Hellmich et al. 1999) improved the approach proposed in (Zachow 1995) as regards both structural modeling (from the aforementioned beam model to 3D) and material modeling of shotcrete. The structural model used in (Hellmich et al. 1999) consists of a ring of 1 m width, fictitiously cut out of the tunnel shell (see Figure 3). This ring contains one MCS. It is discretized by means of 3D finite elements. In the context of nonlinear FE analyses, the displacements at the outer surfaces of the ring are prescribed. They are obtained from interpolation between displacements available at the MPs. The performance of this structural model in the context of hybrid analyses was demonstrated for a MCS at the Sieberg tunnel in Lower Austria (Hellmich et al. 1999). More recently, a similar structural model was employed for the hybrid analysis of segmented tunnel linings of the Semmering pilot tunnel, Austria (Lackner et al. 2001).

The main advantage of the structural model proposed by (Hellmich et al. 1999) is the possibility to account for *in situ* conditions such as, e.g., the actual displacements, the shotcrete mixture used, the air

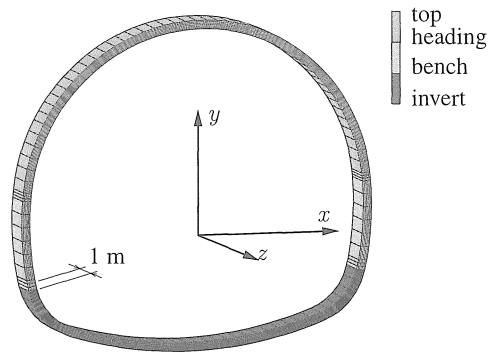


Figure 3: Hybrid method for the analysis of shotcrete shells: structural model used in (Hellmich, Mang, and Ulm 1999) for the analysis of the Sieberg tunnel

temperature, and the actual thickness of the shell. The required nonlinear FE analysis, however, is very time consuming, rendering real-time analyses of shotcrete shells impossible.

The structural model proposed in this paper was developed aiming at *real-time* applications of the hybrid method on site. Similar to the structural model used in (Hellmich et al. 1999), consideration of *in situ* conditions is possible. It is characterized by several simplifications concerning the deformation and stress state of the shotcrete shell. These simplifications are described by means of the following hypotheses:

- H1: The *change of the longitudinal curvature of a shell section is negligible.*
- H2: A *smooth displacement field* is assumed between the MPs. As long as the tunnel shell does not collapse (which would result in a localization of displacements), this is a reasonable assumption.
- H3: *Perfect bond is assumed between the shotcrete shell and the surrounding rock.* The NATM aims at this type of bond: Shotcrete is sprayed onto the more or less rough rock surface, and rock bolts are set in order to support the rock-shotcrete-bond.
- H4: During the deformation, the *thickness of the shell is assumed to be constant.* Because of the small thickness of the shell, this assumption is reasonable.
- H5: Lines which are perpendicular to the interior surface of the tunnel shell right after installation, remain perpendicular to the interior surface during the deformation. Because of the small thickness of the shell, this assumption is reasonable.
- H6: Only axial stresses in the circumferential and longitudinal direction are considered. Since shotcrete shells are loaded predominantly by bi-axial stress states stemming from circumferential and longitudinal deformations, this assumption is reasonable.

Hypotheses H1 to H3 are similar to the ones employed in (Hellmich et al. 1999). They are used to specify the mode of interpolation of displacements between the MPs.

The additional hypotheses H4 and H5 allow determination of the displacement of any point of the shell at any time from *in situ* measured displacements *only*. For this purpose, temporal and spatial interpolation of displacements between the available displacements at the MPs is performed (Hellmich et al. 1999). The displacement field obtained from interpolation is de-

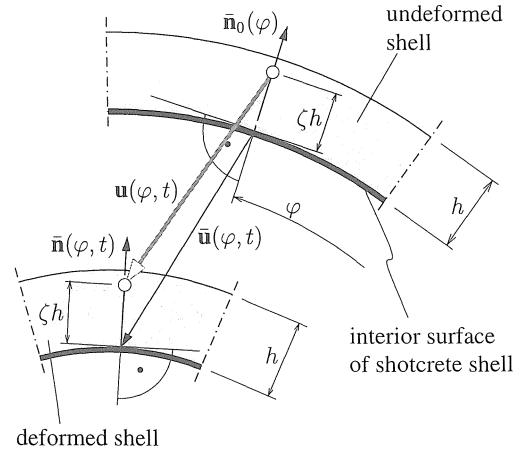


Figure 4: Proposed structural model for hybrid analyses of tunnel shells: illustration of the determination of the displacements of a point of the shotcrete shell,  $\mathbf{u}$ , from the given displacements at the interior surface of the shell,  $\bar{\mathbf{u}}$ , using hypotheses H4 and H5

noted as  $\bar{\mathbf{u}}(\varphi, t)$ , where  $\varphi$  is the circumferential coordinate of the tunnel section.  $\bar{\mathbf{u}}(\varphi, t)$  is prescribed at the interior surface of the tunnel shell, see Figure 4. In this figure, determination of the displacement vector of a point of the shotcrete shell,  $\mathbf{u}$ , on the basis of hypotheses H4 and H5 is illustrated.  $\mathbf{u}$  is obtained from geometric considerations as

$$\mathbf{u}(\varphi, t, \zeta) = -\zeta h \bar{\mathbf{n}}_0(\varphi) + \bar{\mathbf{u}}(\varphi, t) + \zeta h \bar{\mathbf{n}}(\varphi, t), \quad (1)$$

where  $\zeta$  is a normalized coordinate perpendicular to the interior surface of the tunnel shell.  $\bar{\mathbf{n}}_0$  denotes the direction of the shell section right after installation and  $\bar{\mathbf{n}}$  is the respective direction in the deformed configuration. Both  $\bar{\mathbf{n}}_0$  and  $\bar{\mathbf{n}}$  are perpendicular to the interior surface of the tunnel shell (hypothesis H5), i.e., both can be computed from the given displacement field  $\bar{\mathbf{u}}(\varphi, t)$ .

In contrast to the structural model employed in (Hellmich et al. 1999), no FE analysis is required. Hence, the main drawbacks known from nonlinear FE analyses such as high computational cost and partially lacking of robustness do not apply for the proposed structural model, finally paving the way to *real-time* analysis of shotcrete shells on site.

## 2.1 Determination of strains in the shotcrete shell

According to hypothesis H6, only axial stresses in the circumferential and longitudinal direction are considered. The determination of the respective strains from the given displacement field is described in the following.

### 2.1.1 Axial strain in circumferential direction

For determination of the axial strain in the circumferential direction,  $\varepsilon_\varphi$ , layered beam elements are employed (see Figure 5). These elements are *not* used to discretize the shotcrete shell in order to perform an FE analysis. They serve the purpose of determination of  $\varepsilon_\varphi$  *only*. Accordingly, their location is arbitrary and can be specified by the user. If, e.g. the evolutions of axial forces and bending moments at a certain shell section are of interest, only one finite element which is located at the respective shell section is required. In general, however, the overall structural response is of interest. For this purpose, a user-specified number of elements is distributed equally over the tunnel section, see Figure 6. The distance between adjacent elements is given by  $\Delta\varphi$ . The length of each element, represented by  $\Delta\varphi^e$ , is arbitrary and has to be specified by the user.

Once finite elements are placed along the shotcrete shell, the axial strain in the circumferential direction,  $\varepsilon_\varphi$ , can be computed on the basis of the known displacement field.  $\varepsilon_\varphi$  of the  $k$ -th layer,  $\varepsilon_{\varphi,k}$ , is determined from the displacements of the respective points at the beginning and the end of the middle surface of this layer, see points  $P_1$  and  $P_2$  in Figure 5. According to Equation (1), they are given by

$$\mathbf{u}_{1,k}(t) = -\zeta_k h \bar{\mathbf{n}}_0(\varphi_1) + \bar{\mathbf{u}}(\varphi_1, t) + \zeta_k h \bar{\mathbf{n}}(\varphi_1, t) \quad (2)$$

and

$$\mathbf{u}_{2,k}(t) = -\zeta_k h \bar{\mathbf{n}}_0(\varphi_2) + \bar{\mathbf{u}}(\varphi_2, t) + \zeta_k h \bar{\mathbf{n}}(\varphi_2, t). \quad (3)$$

The strain  $\varepsilon_{\varphi,k}$  is computed as

$$\varepsilon_{\varphi,k} = \frac{\ell_k - \ell_{0,k}}{\ell_{0,k}}, \quad (4)$$

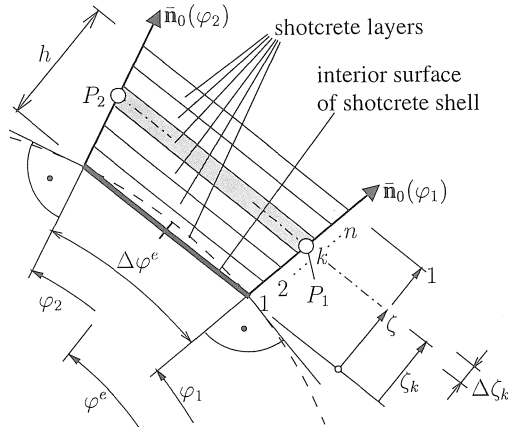


Figure 5: Proposed structural model for hybrid analyses of tunnel shells: layered beam element shown in the undeformed configuration used for determination of the axial strain in the circumferential direction where  $\ell_{0,k}$  and  $\ell_k$  denote the length of the  $k$ -th layer right after installation of shotcrete and in the de-

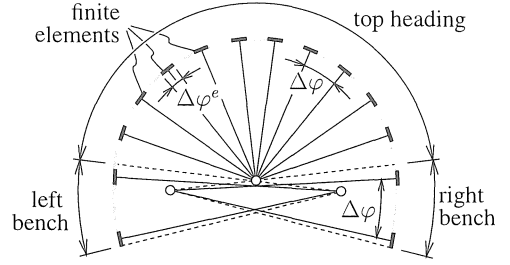


Figure 6: Proposed structural model for hybrid analyses of tunnel shells: equally distributed finite elements for the example of the Sieberg tunnel in Lower Austria

formed configuration, respectively. They are computed from the coordinates of points  $P_1$  and  $P_2$  in the undeformed configuration,  $\mathbf{x}_{1,k}$  and  $\mathbf{x}_{2,k}$ , and the respective displacements given in Equations (2) and (3):

$$\ell_{0,k} = \text{dist}(\mathbf{x}_{1,k}, \mathbf{x}_{2,k}) \quad (5)$$

and

$$\ell_k = \text{dist}(\mathbf{x}_{1,k} + \mathbf{u}_{1,k}, \mathbf{x}_{2,k} + \mathbf{u}_{2,k}). \quad (6)$$

### 2.1.2 Axial strain in longitudinal direction

The axial strain in the longitudinal direction,  $\varepsilon_z$ , is determined by means of interpolation between the measured displacement components in the longitudinal direction at the MPs, such as  $u_{z,MPi}$  for the  $i$ -th MP. The interpolation is based on the value of  $u_{z,MPi}$  at the *considered*, the *previous*, and the *subsequent* MCS, using linear and quadratic interpolation functions, giving  $u_{z,MPi}(z, t)$ , where  $z$  is measured from the *considered* MCS in the direction of the tunnel advance. The strain in the longitudinal direction at the *considered* MCS ( $z = 0$ ) is computed from

$$\varepsilon_{z,MPi}(t) = \varepsilon_z(\varphi = \varphi_{MPi}, t) = \left. \frac{du_{z,MPi}(z, t)}{dz} \right|_{z=0}. \quad (7)$$

$\varepsilon_z$  is determined at the midpoint of the beam elements, given by  $\varphi^e = (\varphi_1 + \varphi_2)/2$  (see Fig. 5). For this purpose, an interpolation between the axial strains at the MPs  $\varepsilon_{z,MPi}(t)$  is performed (see (Hellmich et al. 1999)).

According to hypothesis H1,  $\varepsilon_z$  is constant for all layers of a beam element.

## 3 MULTI-SURFACE CHEMOPLASTICITY MODEL FOR SHOTCRETE

The thermochemoplastic material model for shotcrete is formulated within the framework of thermodynamics of reactive porous media. It is based on a *macroscopic* description of phenomena on the *microlevel* of the material by means of *state variables*. In the material model according to (Hellmich et al. 1999) (Sercombe et al. 2000), two external (macroscopically

measurable) variables ( $\varepsilon$  and  $T$ ) and six internal variables ( $\xi$ ,  $\varepsilon^p$ ,  $\chi$ ,  $\varepsilon^v$ ,  $\varepsilon^f$ , and  $\gamma$ ) are used.

- $\varepsilon$  denotes the strain tensor.
- $T$  stands for the absolute temperature.
- The degree of hydration,  $\xi$ , describes the state of hydration. Hydration is the chemical reaction between cement and free water. The reaction products are termed hydrates.  $\xi$  is the ratio between the current specific mass of water bound in hydrates,  $m$ , and the respective mass at complete hydration,  $m_\infty$ .
- $\varepsilon^p$  and  $\chi$  denote the tensor of plastic strains and the vector of hardening variables, respectively. They represent deformations and microstructural changes because of microcracking, respectively.
- According to Ruetz (Ruetz 1966), the reason for short-term creep are stress-induced movements of water in the capillary pores of concrete. Their diameter is in the range of micrometers. The resulting viscous strains are denoted by  $\varepsilon^v$ .
- According to Wittmann (Wittmann 1982), long-term or flow creep follows from dislocation-like processes in the nanopores of cement gel. Thus, the observation scale of this phenomena is 1000 times smaller than the one concerning short-term creep. The corresponding macroscopic flow strains are denoted by  $\varepsilon^f$ . The internal variable  $\gamma$ , called viscous slip (Ulm 1998), represents microstructural changes resulting from dislocation-like phenomena.

During hydration of shotcrete, new hydrates are formed in a state free of microstress (Bažant 1979). This is reflected by an infinitesimal stress-strain law, reading (Sercombe et al. 2000),

$$d\sigma = \mathbf{C}(\xi) : [d\varepsilon - d\varepsilon^p - \mathbf{1}d\varepsilon^s(\xi) - \mathbf{1}\alpha_T dT - d\varepsilon^v - d\varepsilon^f], \quad (8)$$

with  $\mathbf{C}(\xi)$  as the (aging) isotropic elasticity tensor, depending on Young's modulus  $E(\xi)$  and on a (constant) Poisson's ratio  $\nu$ .  $\mathbf{1}\varepsilon^s(\xi)$  represents the strains caused by chemical shrinkage with  $\mathbf{1}$  as the second-order volumetric unity tensor.  $\alpha_T$  is the coefficient of thermal dilation, which is assumed to be constant. The 1D rheological model depicted in Figure 7 illustrates the employed infinitesimal formulation of the stress-strain law (8): Each hydrate is loaded exclusively by microstress resulting from macrostress applied after the formation of the respective hydrate.

### 3.1 Yield surfaces

The ductile behavior of shotcrete subjected to a multiaxial state of compressive stresses is accounted for

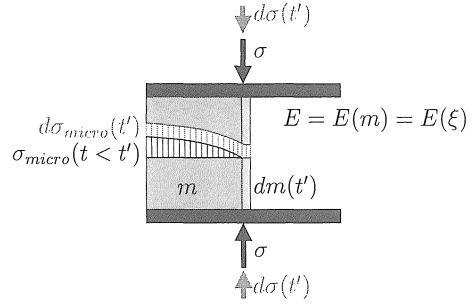


Figure 7: Material model for shotcrete: 1D rheological model illustrating elastic properties of hydrating concrete ( $m$ : specific mass of hydrates formed;  $\sigma_{micro}$ : microstress in the hydrates;  $\sigma$ : macroscopic stress used in the material model;  $E$ : aging Young's modulus)

by a hardening Drucker-Prager model. This material model is suitable for the simulation of predominantly biaxial stress states (see, e.g. (Lackner 2000) (Feenstra 1993)). According to hypothesis H6, only axial stresses in the circumferential and longitudinal direction of the tunnel shell,  $\sigma_\varphi$  and  $\sigma_z$ , are considered. The respective form of the Drucker-Prager criterion is given as

$$f_D(\sigma_\varphi, \sigma_z, \zeta_D) = \sqrt{J_2} + \alpha I_1 - \zeta_D(\chi_D, \xi)/\beta, \quad (9)$$

with

$$I_1 = \sigma_\varphi + \sigma_z, \quad J_2 = \frac{1}{3} (\sigma_\varphi^2 - \sigma_\varphi \sigma_z + \sigma_z^2). \quad (10)$$

In Equation (9),  $\zeta_D$  is the hardening force which in case of chemoplasticity depends on both the hardening variable  $\chi_D$  and the state of the chemical reaction represented by  $\xi$ .  $\alpha$  and  $\beta$  are material parameters.

Microcracking of shotcrete is modelled by means of the maximum tensile stress (Rankine) criterion. According to hypothesis H6, two Rankine criteria are employed to control the tensile stresses of shotcrete in the circumferential and longitudinal direction:

$$f_{R,\varphi}(\sigma_\varphi, \zeta_{R,\varphi}) = \sigma_\varphi - \zeta_{R,\varphi}(\chi_{R,\varphi}, \xi) \quad (11)$$

and

$$f_{R,z}(\sigma_z, \zeta_{R,z}) = \sigma_z - \zeta_{R,z}(\chi_{R,z}, \xi). \quad (12)$$

$\zeta_{R,\varphi}$  and  $\zeta_{R,z}$  are the respective hardening forces. The use of two hardening forces allows consideration of cracking in the circumferential and longitudinal direction as two independent processes. Hence, in contrast to isotropic softening, the strength in one direction remains unchanged when the crack in the other direction is opening. This agrees with experimental observations.

The employed yield surfaces define the space of admissible stress states, given by

$$\sigma \in C_E \leftrightarrow \begin{cases} f_D(\sigma_\varphi, \sigma_z, \zeta_D) \leq 0, \\ f_{R,\varphi}(\sigma_\varphi, \sigma_z, \zeta_{R,\varphi}) \leq 0, \\ f_{R,z}(\sigma_\varphi, \sigma_z, \zeta_{R,z}) \leq 0. \end{cases} \quad (13)$$

Figure 8 shows this space in the  $\sigma_\varphi$ - $\sigma_z$  stress space.

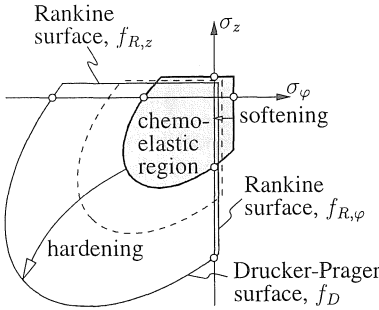


Figure 8: Material model for shotcrete: illustration of employed yield surfaces in the  $\sigma_\varphi$ - $\sigma_z$  stress space

### 3.2 Hardening/softening laws – calibration

The material parameters  $\alpha$  and  $\beta$  of the Drucker-Prager criterion can be determined by means of the uniaxial compressive strength  $f_c$  and the biaxial compressive strength  $f_b$ . Experimental results (Byfors 1980) suggest the assumption of isotropic chemical hardening. In this case, the ratio  $\kappa = f_b/f_c \approx 1.16$  remains constant during hydration. Inserting the two pairs of stresses given for a uniaxial and a biaxial compressive test,  $(-f_c, 0)$  and  $(-f_b, -f_b)$ , into (9),  $\alpha$  and  $\beta$  are obtained as

$$\alpha = \frac{\kappa - 1}{\sqrt{3}(2\kappa - 1)} \quad \text{and} \quad \beta = \frac{\sqrt{3}(2\kappa - 1)}{\kappa}. \quad (14)$$

Employing a quadratic plastic hardening law,  $\zeta_D$  can be expressed as (see Figure 9)

$$\zeta_D(\chi_D, \xi) = \begin{cases} \omega f_c(\xi) + [f_c(\xi) - \omega f_c(\xi)] \left[ 1 - \frac{(\chi_D - \bar{\chi}_D)^2}{\bar{\chi}_D^2} \right] & \dots \text{ for } \chi_D < \bar{\chi}_D, \\ f_c(\xi) & \dots \text{ for } \chi_D \geq \bar{\chi}_D, \end{cases} \quad (15)$$

where  $\omega$  denotes the ratio between the elastic limit under uniaxial compressive loading,  $f_y$ , and the compressive strength  $f_c$ :  $\omega = f_y/f_c \approx 0.25$ . Similar to  $\kappa$ ,  $\omega$  remains constant during hydration.  $\bar{\chi}_D$  can be determined from a uniaxial compression test at complete hydration,

$$\bar{\chi}_D = \varepsilon_{c,\infty}^u - f_{c,\infty}/E_\infty, \quad (16)$$

where  $\varepsilon_{c,\infty}^u$  represents the total strain at peak stress, with  $\varepsilon_{c,\infty}^u \approx 0.0022$ .  $f_{c,\infty}$  and  $E_\infty$  are the final values

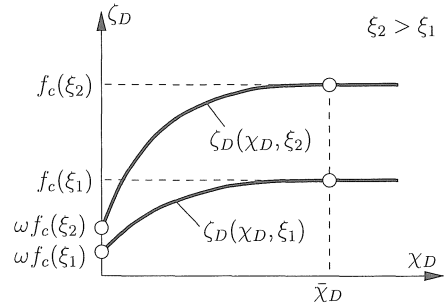


Figure 9: Material model for shotcrete: increase of  $\zeta_D$  in consequence of microcracking (strain hardening) for two different values of  $\xi$

of the compressive strength and Young's modulus, respectively.

As regards the Rankine criterion, an infinitesimal formulation is employed for the description of strain softening and chemical hardening, reading (Lackner & Mang 2001)

$$d\zeta_{R,\varphi} = d\zeta_{R,\varphi}(d\chi_{R,\varphi}, d\xi) \quad (17)$$

and

$$d\zeta_{R,z} = d\zeta_{R,z}(d\chi_{R,z}, d\xi). \quad (18)$$

In contrast to the commonly used total formulation, characterized by  $\zeta = \zeta(\chi, \xi)$ , the increase of strength in consequence of hydration (chemical hardening) is added directly to the actual strength and does not depend on  $\chi$ , i.e. does not depend on the state of microcracking (partial decoupling hypothesis). According to (Lackner & Mang 2001), only the infinitesimal formulation gives the correct amount of released energy in consequence of early-age fracture. For the case of purely chemical hardening, characterized by  $\zeta = \zeta(\xi)$ , the total and infinitesimal formulation give the same result.

The finite counterpart of the infinitesimal formulation for the hardening force  $\zeta_{R,\varphi}$  (17) for the  $(n+1)$ -st load increment reads (see Fig. 10)

$$\Delta\zeta_{R,\varphi,n+1} = \underbrace{\zeta_{R,\varphi,n+1}^{tr} \left[ 1 - \exp\left(-\frac{\Delta\chi_{R,\varphi,n+1}}{\bar{\chi}_{R,\varphi,n+1}}\right) \right]}_{\text{strain softening}}, \quad (19)$$

with

$$\zeta_{R,\varphi,n+1}^{tr} = \zeta_{R,\varphi,n} + \underbrace{\Delta\zeta_{R,\varphi,n+1}^{hyd}}_{\text{chemical hardening}}(\Delta\xi_{n+1}). \quad (20)$$

In Equation (20),  $\Delta\zeta_{R,\varphi,n+1}^{hyd}$  represents the increase of tensile strength in consequence of chemical hardening. It is computed from the incremental increase of the degree of hydration,  $\Delta\xi_{n+1}$ . The calibration parameter  $\bar{\chi}_{R,\varphi,n+1}$  in Equation (19) accounts for the

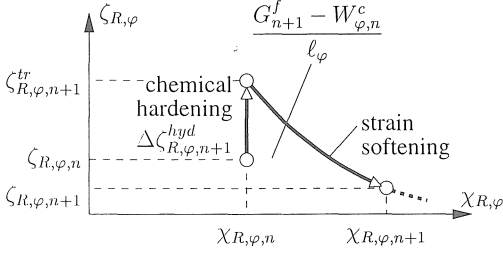


Figure 10: Material model for shotcrete: illustration of the incremental change of  $\zeta_{R,\varphi}$  for the  $(n + 1)$ -st load (time) increment consisting of chemical hardening and strain softening

energy related to crack opening. This energy is given by the difference between the fracture energy  $G_{n+1}^f$  and the energy released in previous load (time) increments,  $W_{\varphi,n}^c$ .  $\bar{\chi}_{R,\varphi,n+1}$  is computed from

$$G_{n+1}^f - W_{\varphi,n}^c = \ell \int_0^\infty \zeta_{R,\varphi,n+1}^{tr} \exp\left(-\frac{\Delta\chi_{R,\varphi}}{\bar{\chi}_{R,\varphi,n+1}}\right) d(\Delta\chi_{R,\varphi}), \quad (21)$$

where  $\ell$  denotes the average spacing between adjacent opening cracks (determination of  $\ell$  is described in the following subsection). Integration of (21) gives the calibration parameter  $\bar{\chi}_{R,\varphi,n+1}$  as

$$\bar{\chi}_{R,\varphi,n+1} = \frac{G_{n+1}^f - W_{\varphi,n}^c}{\zeta_{R,\varphi,n+1}^{tr} \ell} \quad (22)$$

with  $G_{n+1}^f = G_n^f + \Delta G^f(\Delta\xi_{n+1})$ .

### 3.3 Consideration of reinforcement

As known from reinforced concrete design (CEB-FIP 1990), the presence of reinforcement leads to a distribution of cracks finally forming a stabilized crack pattern (see Fig. 11). The formation of a stabilized crack pattern has already been accounted for by the average crack spacing  $\ell$  in the determination of the calibration parameter  $\bar{\chi}_{R,\varphi,n+1}$  (Eqn. (22)). The interaction between the reinforcement bars and the surrounding shotcrete, the so-called tension stiffening effect, results in an increase of stiffness and strength of the composite material. In the present model, the tension stiffening effect is considered within the material model for shotcrete by increasing the fracture energy by the factor  $\gamma$ , with  $\gamma > 1$ . Hence, the tension stiffening effect is considered in the analysis model for strain softening.

Both the average crack spacing  $\ell$  and the factor  $\gamma$  depend on the material properties of shotcrete and steel and the geometric properties as the shotcrete cover  $c$ , the effective tension height for shotcrete,  $h_{c,eff}$ , and the reinforcement ratio, given by  $\rho_s =$

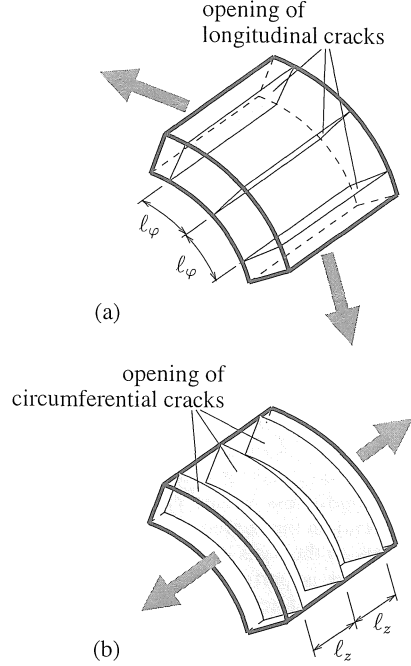


Figure 11: Material model for reinforced shotcrete: illustration of cracks opening in shotcrete shells showing the average crack spacing in the circumferential and longitudinal direction,  $\ell_\varphi$  and  $\ell_z$

$a_s/h_{c,eff}$ . For the case of two layers of reinforcement such as used in shotcrete tunnel shells, the effective tension height can be estimated according to (CEB-FIP 1990) (see Figure 12):

$$h_{c,eff} = \min\{2.5(c + \phi_s/2), h/2\}, \quad (23)$$

with  $\phi_s$  as the diameter of the reinforcement bars.  $\ell$  and  $\gamma$  are computed by means of a 1D composite model (for details on the composite model, see (Lackner 2000) (Lackner & Mang 2000)). The model consists of one steel bar and the surrounding shotcrete.

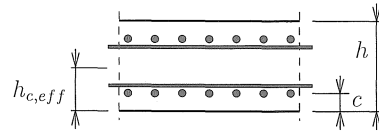


Figure 12: Material model for reinforced shotcrete: on the evaluation of the effective tension height for shotcrete,  $h_{c,eff}$ , for reinforced shotcrete shells

For the description of the interaction between steel and shotcrete, a nonlinear bond slip - bond stress relation is considered. This relation is taken from (CEB-FIP 1990) and extended towards aging materials (see Figure 13). Similar to the chemomechanical coupling

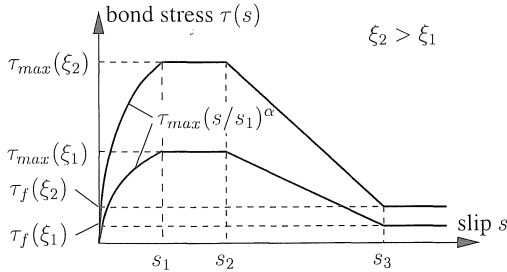


Figure 13: Material model for reinforced shotcrete: bond slip - bond stress relation according to (CEB-FIP 1990) extended towards consideration of aging

used in the hardening law for the Drucker-Prager criterion (see Fig. 9), deformations such as the slip values  $s_1$  to  $s_3$  are assumed to be constant and stresses such as the bond-stress values  $\tau_f$  and  $\tau_{max}$  are assumed to depend on the degree of hydration.

The analysis on the basis of the aforementioned 1D composite model is performed under displacement control. The reaction forces are monitored for the bare steel bar and the embedded steel bar, giving  $p_{bare}$  and  $p_{embedded}$  (see Figure 14). The difference in deformation energy between the embedded and the bare steel bar,

$$\int_0^\infty \frac{p_{embedded} - p_{bare}}{h_{c,eff}} d\bar{u}, \quad (24)$$

where  $\bar{u}$  stands for the prescribed displacement at the crack face, is set equal to  $\gamma G^f$ . The factor  $\gamma$  is considered in the calibration of the Rankine criteria. Hence, Equation (22) becomes

$$\bar{\chi}_{R,\varphi,n+1} = \frac{G_{incr,n+1}^f - W_{\varphi,n}^c}{\zeta_{R,\varphi,n+1}^{tr} \ell}. \quad (25)$$

with  $G_{incr,n+1}^f = G_{incr,n}^f + \gamma(\xi_{n+1})\Delta G^f(\Delta\xi_{n+1})$ .

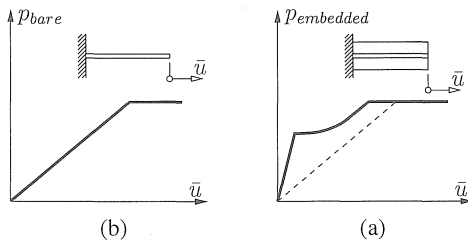


Figure 14: Material model for reinforced shotcrete: illustration of the obtained load-displacement relation of (a) a bare steel bar and (b) an embedded steel bar

### 3.4 Intrinsic material functions

The material properties of shotcrete are related to the degree of hydration  $\xi$  by means of intrinsic material functions. *Intrinsic* means that these functions are

independent of field and boundary conditions. Altogether seven material functions are required for the described material model. They are determined from extended laboratory tests, providing

- the normalized chemical affinity  $\bar{A}$ ,
- the compressive strength  $f_c$ ,
- Young's modulus  $E$ ,
- the chemical shrinkage strain  $\varepsilon^s$ ,
- the characteristic time for short-term creep,  $\tau_w$ ,
- the final viscous compliance  $J_{\infty}^v$ , and
- the fracture energy  $G^f$

as functions of the degree of hydration  $\xi$ .

The intrinsic function for the normalized chemical affinity,  $\bar{A}(\xi)$ , is depicted in Figure 15(a) for a shotcrete mixture investigated at Lafarge CTEC Mannersdorf, see (Hellmich 1999). In order to facilitate the implementation of the normalized chemical affinity  $\bar{A}$  in the numerical analyses, an analytical expression is established:

$$\bar{A}(\xi) = a \frac{1 - \exp(-b\xi)}{1 + c\xi^d}. \quad (26)$$

For the evaluation of the free parameters  $a$ ,  $b$ ,  $c$ , and  $d$ , a nonlinear regression is performed (Hellmich 1999). Figure 15(b) shows the linear strength growth of concrete/shotcrete (Mindess et al. 1978). The final strength of the considered Lafarge shotcrete is 39.6 MPa. In Figure 15(b),  $\xi_0$  denotes the percolation threshold (Acker 1988) beyond which the material can support a stress deviator. The evolution of Young's modulus  $E(\xi)$  for this shotcrete is given in Figure 15(c). The intrinsic function for chemical shrinkage strains is depicted in Figure 15(d). It was computed from experiments conducted by (Huber 1991). Figure 15(e) shows the employed linear intrinsic function for the characteristic time for short-term creep. The final value of  $\tau_w$ ,  $\tau_{w,\infty}$ , for the considered Lafarge shotcrete is approximately 24 hours (Hellmich 1999). For the same shotcrete,  $J_{\infty}^v(\xi)$  is depicted in Figure 15(f) (Lechner et al. 2001). According to (Lackner & Mang 2001) a linear intrinsic function is employed for the fracture energy  $G^f$  (see Figure 15(g)).

## 4 APPLICATION: SIEBERG TUNNEL IN LOWER AUSTRIA

For the numerical analysis of the Sieberg tunnel, the measurement cross-section MCS1452 (km 156.990)

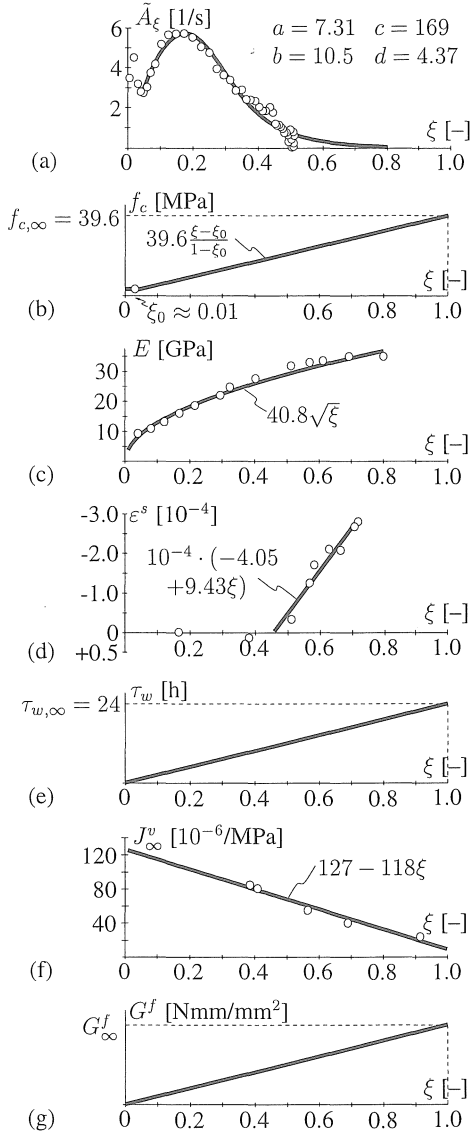


Figure 15: Intrinsic material functions for shotcrete: (a) normalized chemical affinity, (b) strength growth, (c) aging elasticity, (d) chemical shrinkage, (e) characteristic time for short-term creep, (f) final viscous compliance, and (g) fracture energy

is chosen. For evaluation of the axial strains in the longitudinal direction, the *preceding* and the *subsequent* MCS, i.e. MCS1444 (km 156.998) and MCS1462 (km 156.980), are employed.

#### 4.1 Geometric dimensions and material properties

The geometric dimensions of the standard cross-section of the Sieberg tunnel are given in Figure 16.

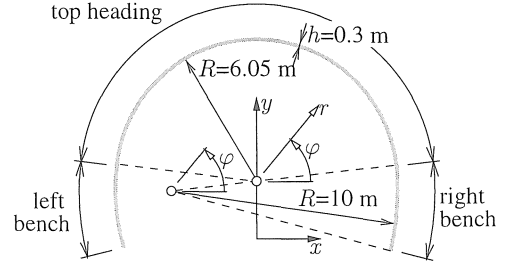


Figure 16: Sieberg tunnel: cross-section

Typical mechanical properties of shotcrete used in the following analysis are listed in Table 1.

Table 1: Sieberg tunnel: mechanical material parameters for shotcrete

final Young's modulus [MPa]	40,800
Poisson's ratio [-]	0.2
final compressive strength $f_{c,\infty}$ [MPa]	39.6
final tensile strength $f_{t,\infty}$	$f_{c,\infty}/10$

The final value of the fracture energy  $G^f$ ,  $G^f_\infty$ , is computed from (CEB-FIP 1990)

$$G^f_\infty = G^f_0 \left( \frac{f_{c,\infty}}{f_{c0}} \right)^{0.7}, \quad (27)$$

where  $f_{c0}=10$  N/mm<sup>2</sup>.  $G^f_0$  depends on the maximum aggregate size  $d_{max}$ . For the maximum aggregate size of shotcrete, namely 8 mm,  $G^f_0$  is obtained as 0.025 Nmm/mm<sup>2</sup> (CEB-FIP 1990), giving  $G^f_\infty = 0.065$  Nmm/mm<sup>2</sup>.

The shotcrete shell is reinforced with two layers of AQ60 (ø6 mm, spacing of 100 mm, giving  $a_s = 283$  mm<sup>2</sup>/m). Assuming a shotcrete cover  $c$  of 30 mm, the effective tensile shotcrete height is obtained as  $h_{c,eff} = 82.5$  mm (Eqn. (23)).

The material functions for the average crack spacing  $\ell$  and the factor  $\gamma$ , which are required for the calibration of the Rankine criteria, are computed on the basis of the earlier-described 1D composite model (see Subsection 3.3). Hereby, the following properties describing the bond slip – bond stress relation (Fig. 13) are used:  $\tau_{max} = 2\sqrt{f_c}$ ,  $\tau_f = 0.15\tau_{max}$ ,  $s_1 = s_2 = 0.6$  mm,  $s_3 = 1.0$  mm, and  $\alpha = 0.4$  (CEB-FIP 1990).  $\ell$  and  $\gamma$  are determined for different values of  $\xi$ , giving discrete values of the functions  $\ell(\xi)$  and  $\gamma(\xi)$  (see circles in Figure 17). The obtained relations are approximated by a constant and a linear function, respectively, as shown in Figure 17.

#### 4.2 Monitoring equipment

Five devices for 3D displacement measurements are installed at each MCS, see Figure 18. The measure-

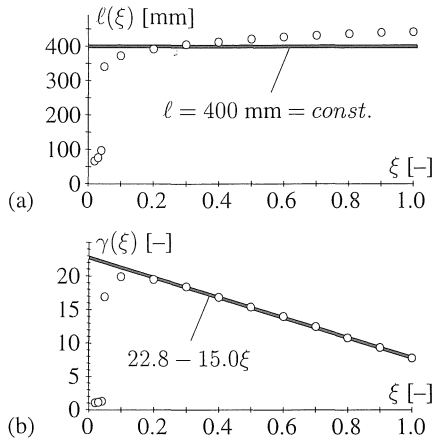


Figure 17: Sieberg tunnel: material functions for the average crack spacing  $\ell$  and the factor  $\gamma$  used for the calibration of the Rankine criteria

ment devices provide displacement vectors. all measured in *one* spatial reference system.

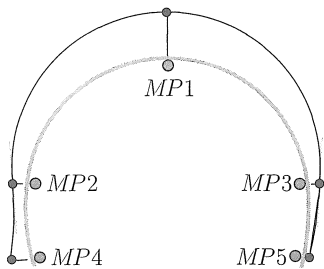


Figure 18: Sieberg tunnel: monitoring equipment consisting of five MPs

### 4.3 Construction history

The construction history for the part of the tunnel around MCS1452 is depicted graphically in Figure 19. 120 h after the erection of the top heading in MCS1452, the construction works were interrupted for 456 h (Christmas vacations). The left and the right bench, respectively, were installed 288 h and 336 h, respectively, after resuming work.

### 4.4 Numerical results – level of loading

For the analysis of the Sieberg tunnel, 31 layered beam elements are employed. They are distributed equally over the circumferential direction of the shotcrete shell, with  $\Delta\varphi = 6.6^\circ$  (see Table 2).  $\Delta\varphi$  represents the distance between the middle points of two adjacent elements. As regards the discretization of the shell over the thickness, six layers, each of 5 cm thickness, are used. The angle giving the length of the beam elements,  $\Delta\varphi^e$  (Fig. 6), is set equal to  $0.01^\circ$ .

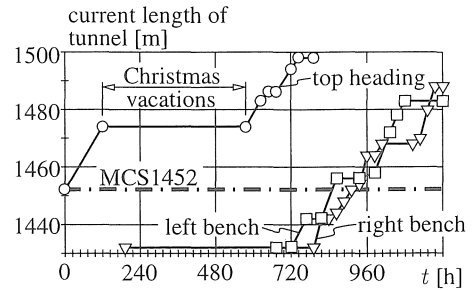


Figure 19: Sieberg tunnel: construction history for top heading, left bench, and right bench ( $t = 0$  refers to the time constant of installation of the top heading)

For the present analysis, isothermal conditions with  $T = 20^\circ\text{C} = \text{const.}$  are assumed.

The time span considered in the analysis is 50 days, starting with the installation of the top heading. The temporal discretization is characterized by time (load) increments of 0.25 h, yielding 4800 time increments. Based on the proposed structural model presented in Section 2, the analysis of the Sieberg tunnel took only two minutes. Needless to say, the analysis on the basis of a fully 3D model would require significantly more computation time.

The state of deformation in the tunnel at the considered MCS is illustrated in Figure 20 by means of the circumferential and the longitudinal stretches,

$$\epsilon_\varphi = \sum_{k=1}^n \epsilon_{\varphi,k} \Delta\zeta_k \quad \text{and} \quad \epsilon_z = \sum_{k=1}^n \epsilon_{z,k} \Delta\zeta_k, \quad (28)$$

Table 2: Sieberg tunnel: location of middle points of layered beam elements

no.	$\varphi$	no.	$\varphi$	no.	$\varphi$	no.	$\varphi$
1	$-9.4^\circ$	9	$43.6^\circ$	17	$96.6^\circ$	25	$149.7^\circ$
2	$-2.8^\circ$	10	$50.2^\circ$	18	$103.3^\circ$	26	$156.3^\circ$
3	$3.8^\circ$	11	$56.8^\circ$	19	$109.9^\circ$	27	$162.9^\circ$
4	$10.4^\circ$	12	$63.5^\circ$	20	$116.5^\circ$	28	$169.6^\circ$
5	$17.1^\circ$	13	$70.1^\circ$	21	$123.2^\circ$	29	$176.2^\circ$
6	$23.7^\circ$	14	$76.7^\circ$	22	$129.8^\circ$	30	$182.8^\circ$
7	$30.3^\circ$	15	$83.4^\circ$	23	$136.4^\circ$	31	$189.5^\circ$
8	$36.9^\circ$	16	$90.0^\circ$	24	$143.1^\circ$		

where  $n$  represents the number of layers. For the finite element located at the top, compressive circumferential stretches prevail (Fig. 20(a)). Remarkably, they are *not* monotonically increasing. At the right footing of the top heading, compressive stretches evolve rapidly reaching their peak approximately 80 hours after installation of the top heading (Fig. 20(b)). This rapid increase is followed by a decrease of almost 70%. In the left bench, the compressive circumferential stretches undergo a reduction of approximately 45% between  $t = 960$  and  $1090$  h (Fig. 20(c)). For

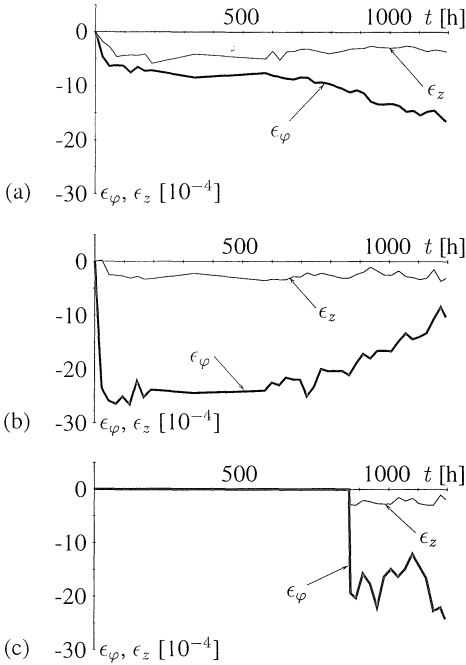


Figure 20: Sieberg tunnel: stretches  $\epsilon_\varphi$  and  $\epsilon_z$  at MCS1452 at (a)  $\varphi = 90^\circ$  (element 16), (b)  $\varphi = 10.4^\circ$  (element 4), and (c)  $\varphi = 182.8^\circ$  (element 30)

$t > 1090$  h, an increase of  $\epsilon_\varphi$  is observed. The longitudinal stretches are lying within the compressive regime. They are significantly smaller than  $\epsilon_\varphi$ .

Figure 21 shows the evolution of the axial forces in the circumferential and the longitudinal direction,

$$n_\varphi = \sum_{k=1}^n \sigma_{\varphi,k} h \Delta \zeta_k \quad \text{and} \quad n_z = \sum_{k=1}^n \sigma_{z,k} h \Delta \zeta_k. \quad (29)$$

After application of the top heading, compressive circumferential forces develop (Fig. 21(a)). These forces are simultaneously reduced by the creep capacities of shotcrete. During the Christmas vacations, the stress relaxation continues ( $200 < t < 330$  h). At  $t = 330$  h, the compressive circumferential stretches  $\epsilon_\varphi$  slightly decrease (Fig. 20(a)). Temporarily, this results in tensile forces in the top heading. Continuation of the excavation after the Christmas vacations again leads to compressive loading states in the circumferential direction of the shotcrete shell. At the right footing of the top heading, the rather abrupt increase of the compressive stretches  $\epsilon_\varphi$  (Fig. 20(b)) leads to high compressive loading of the young shotcrete. From  $t = 100$  to 570 h the evolution of  $\epsilon_\varphi$  is almost constant. The creep properties of shotcrete, however, result in a relaxation of the compressive stresses. The reduction of  $\epsilon_\varphi$  for  $t > 570$  h leads to tensile loading causing cracking of shotcrete. At  $t = 600$  h, the employed Rankine

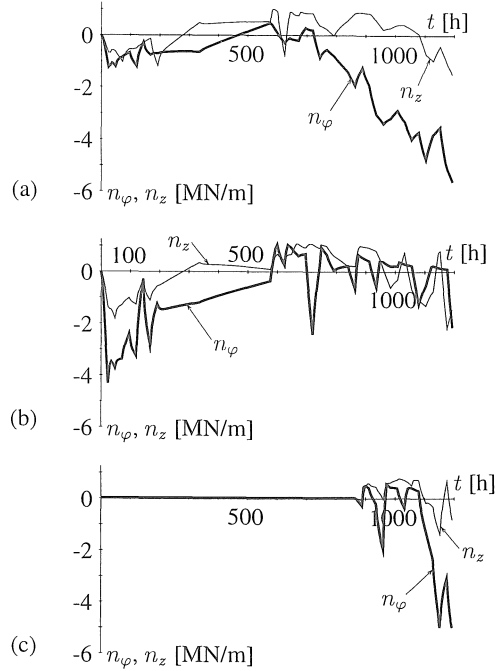


Figure 21: Sieberg tunnel: axial forces in circumferential and longitudinal direction,  $n_\varphi$  and  $n_z$ , at MCS1452 at (a)  $\varphi = 90^\circ$  (element 16), (b)  $\varphi = 10.4^\circ$  (element 4), and (c)  $\varphi = 182.8^\circ$  (element 30)

criterion gives a good estimate of the maximum tensile load in the circumferential direction, which can be carried by the shell, i.e.  $n_{\varphi,max} \approx f_{t,\infty} h = 4 \cdot 0.3 = 1.2$  MN/m, where  $f_{t,\infty} = 4$  MN/m<sup>2</sup> represents the tensile strength at the end of hydration. For  $t > 600$  h, the tensile force that can be carried by the shotcrete is decreasing as a consequence of strain softening. In the left bench, the reduction of compressive circumferential stretches observed in Figure 20(b) between 960 and 1080 hours results in tensile loading (Fig. 21(c)). For  $t > 1080$  h, the increase of the circumferential compressive stretches leads to compressive loading of the left bench.

As regards the axial force in the longitudinal direction,  $n_z$ , realistic modelling of chemical shrinkage in the material model for shotcrete together with the decreasing evolution of the compressive longitudinal stretch  $\epsilon_z$  between 200 and 920 hours leads to tensile stresses in the top heading (Fig. 21(a)). A similar response in the longitudinal direction is observed at the right footing of the top heading (Fig. 21(b)). Right after installation of the left bench, chemical shrinkage results in tensile loading of shotcrete in the longitudinal direction (Fig. 21(c)). Again, the used Rankine criterion is well-suited for the representation of cracking in the shotcrete shell.

In order to assess the crack opening in the tunnel

shell, crack indicators  $C_\varphi$  and  $C_z$  are introduced in the form

$$C_\varphi = \frac{W_\varphi^c(t)}{G_{incr}^f(t)} \quad \text{and} \quad C_z = \frac{W_z^c(t)}{G_{incr}^f(t)}. \quad (30)$$

$C_\varphi$  and  $C_z$  relate the released energy in consequence of cracking,  $W_\varphi^c$  and  $W_z^c$ , to the increased fracture energy  $G_{incr}^f$ . Hence, for values of  $C$  equal to zero, no cracking has occurred so far. For  $C = 1$ , all hydrates at the crack face are broken, giving a tensile strength equal to zero. Figure 22 shows the evolutions of

$$\bar{C}_\varphi = \sum_{k=1}^n C_\varphi^k \Delta \zeta^k \quad \text{and} \quad \bar{C}_z = \sum_{k=1}^n C_z^k \Delta \zeta^k \quad (31)$$

for the FE elements located at  $\varphi = 90^\circ$ ,  $10.4^\circ$ , and  $182.8^\circ$ .  $\bar{C}_\varphi = 0$  at the top of the tunnel shell (Fig. 22(a)) indicates that the observed circumferential deformations do not cause cracking of shotcrete. At  $\varphi = 10.4^\circ$  and  $182.8^\circ$ , however, the reduction of the compressive stretches  $\epsilon_\varphi$  causes cracking. Almost every time, when  $\epsilon_\varphi$  is reduced, an increase of  $\bar{C}_\varphi$  is observed in Figures 22(b) and 22(c). At  $t = 1200$  h,  $\bar{C}_\varphi$  at the right footing of the top heading is equal to 91.3% (Fig. 22(b)). The respective decrease of the tensile load-carrying capacity is reflected in the evolution of  $n_\varphi$  shown in Figure 21(b). The compressive stretches in the longitudinal direction at the top of the tunnel shell are neither constant nor monotonically increasing (Fig. 20(a)). Hence, in time intervals characterized by a reduction of the compressive longitudinal stretches ( $570 < t < 700$  h, see Fig. 20(a)), cracking of shotcrete occurs as indicated by the evolution of  $\bar{C}_z$  (Fig. 22(a)). Similar to the evolutions of  $\bar{C}_z$  at  $\varphi = 10.4^\circ$  and  $182.8^\circ$ ,  $\bar{C}_z$  at  $\varphi = 90^\circ$  does not exceed 30%. Hence, at least 70% of the formed hydrates are still intact, providing the observed residual tensile strength of shotcrete in the longitudinal direction (Fig. 21).

Finally, the level of loading,  $L$ , is evaluated. It amounts to 0% for the structure without loads and to 100% when the (actual) compressive strength is reached. For the Drucker-Prager criterion, the level of loading for the  $k$ -th layer is given as

$$L_k = \frac{\sqrt{J_2(\sigma_{\varphi,k}, \sigma_{z,k})} + \alpha I_1(\sigma_{\varphi,k}, \sigma_{z,k})}{f_c(\xi_k)/\beta}, \quad (32)$$

see Figure 23.

in the tunnel cross-section. Right after installation of the top heading, values for  $\bar{L}$  up to 80% are obtained at the footings of the top heading. This reflects the earlier-observed abrupt increase of compressive circumferential stretches  $\epsilon_\varphi$  and of the respective axial force  $n_\varphi$  (see Figs. 20(b) and 21(b)). With increasing

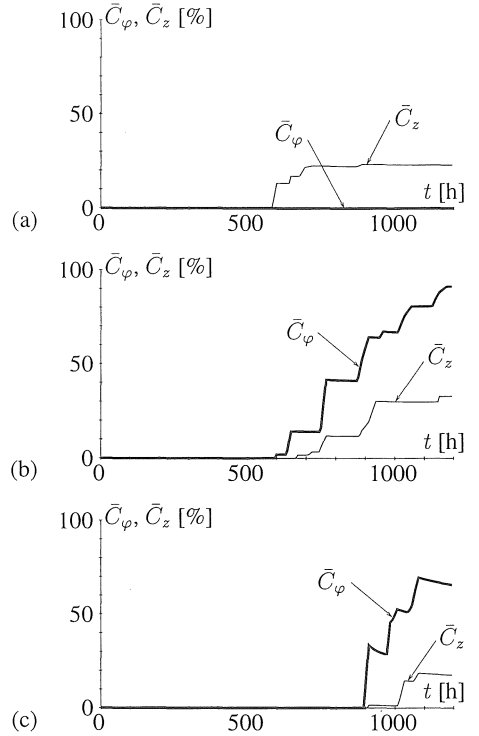


Figure 22: Sieberg tunnel: crack indicators  $\bar{C}_\varphi$  and  $\bar{C}_z$  at MCS1452 at (a)  $\varphi = 90^\circ$  (element 16), (b)  $\varphi = 10.4^\circ$  (element 4), and (c)  $\varphi = 182.8^\circ$  (element 30)

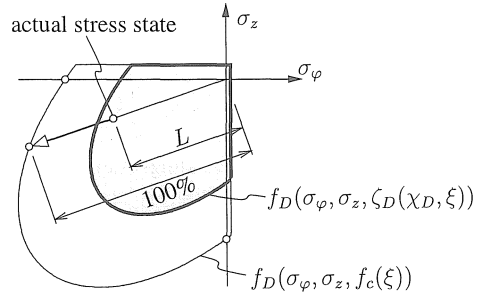


Figure 23: Sieberg tunnel: illustration of the level of loading  $L$  in the  $\sigma_\varphi$ - $\sigma_z$  stress space

time, relaxation in consequence of creep of shotcrete results in a reduction of  $\bar{L}$  below 20% for the entire top heading, see calendar week 2, 1998 in Figure 24. Installation of the benches, however, causes further loading of the shell reflected by the increase of  $\bar{L}$  in the top heading to a value of 40.1%. The increase of the compressive circumferential stretches  $\epsilon_\varphi$  in the left bench for  $t > 1090$  h (Fig. 20(c)) yields very large values of  $\bar{L}$ . The maximum value is obtained at the footing of the left bench as  $\bar{L} = 95.4\%$ .

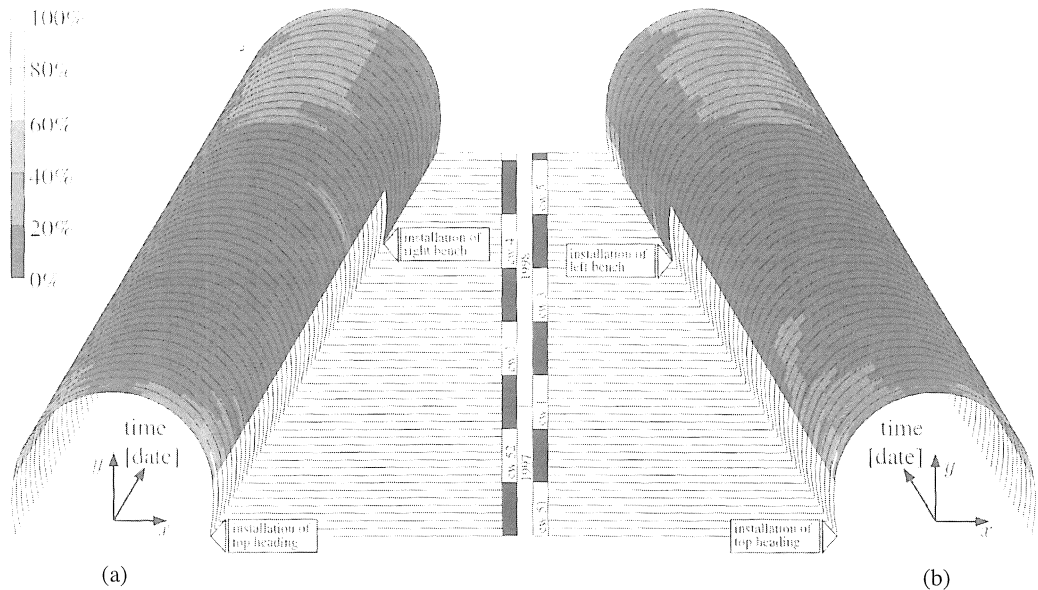


Figure 24: Evolution of  $\bar{L}$  of the Sieberg tunnel at MCS1452: (a) right view and (b) left view (cw: calendar week)

Figure 24 shows the evolution of  $\bar{L}$ , where

$$\bar{L} = \sum_{k=1}^n L_k \Delta \zeta_k, \quad (33)$$

## 5 CONCLUSIONS

An efficient and robust analysis tool for quantification of the stress state in shotcrete tunnel shells was presented. It is based on the combination of *in situ* displacement measurements and a material model for shotcrete. In addition to commonly considered material properties of shotcrete, such as aging, creep, and plasticity, the material model was extended to account for early-age fracture of shotcrete. The interaction between the reinforcement of the tunnel lining and the surrounding shotcrete was considered in the calibration of the shotcrete model.

From hybrid analysis of the Sieberg tunnel the following conclusions can be drawn:

- Right after installation of the top heading, high compressive loading was encountered at the footings, characterized by a level of loading up to 80%.
- The installation of the benches caused an increase of the loading of the tunnel shell which was reflected by an increase of the level of loading in the top heading.

- Cracking in both the circumferential and the longitudinal direction was indicated by the analysis. The main reasons for cracking are reductions of compressive circumferential and longitudinal stretches in the shell and shrinkage of shotcrete. The employed Rankine criterion together with the proposed mode of calibration allowed the simulation of strain softening in consequence of microcracking, crack healing, and the interaction between the reinforcement and shotcrete.

The analysis of the Sieberg tunnel took less than two minutes for a simulation time of 50 days. Hence, the proposed strategy is well-suited for on-line monitoring of stress states in tunnel shells *on site*.

## REFERENCES

- Acker, P. (1988). Comportement mécanique du béton: apports de l'approche physico-chimique [Mechanical behavior of concrete: a physico-chemical approach]. Technical Report Res. Rep. LCPC 152, Laboratoires des Ponts et Chaussées, Paris, France. In French.
- Bazant, Z. (1979). Thermodynamics of solidifying or melting viscoelastic material. *Journal of the Engineering Mechanics Division, ASCE* 105(6), 933–952.
- Byfors, J. (1980). Plain concrete at early ages. Technical report, Swedish Cement and Concrete Research Institute, Stockholm, Sweden.

- CEB-FIP (1990). *Model Code 1990, Bulletin d'Information*. Lausanne, Switzerland: CEB.
- Coussy, O. (1995). *Mechanics of porous continua*. Chichester, England: Wiley.
- Feenstra, P. (1993). *Computational aspects of biaxial stress in reinforced concrete*. Ph. D. thesis, Technical University Delft, The Netherlands.
- Hellmich, C. (1999). *Shotcrete as part of the New Austrian Tunneling Method: from thermochemomechanical material modeling to structural analysis and safety assessment of tunnels*. Ph. D. thesis, Vienna University of Technology, Vienna, Austria.
- Hellmich, C., H. Mang, and F.-J. Ulm (1999). Hybrid method for quantification of stress states in shotcrete tunnel shells: combination of 3D *in-situ* displacement measurements and thermochemoplastic material law. In W. Wunderlich (Ed.), *CD-ROM Proceedings of the 1st European Conference of Computational Mechanics*, Munich, Germany.
- Hellmich, C., F.-J. Ulm, and H. A. Mang (1999). Multisurface chemoplasticity I: Material model for shotcrete. *Journal of Engineering Mechanics (ASCE)* 125(6), 692–701.
- Hillerborg, A., M. Modeer, and P. Petersson (1976). Analysis of crack formation and crack growth in concrete by means of fracture mechanics and finite elements. *Cement and Concrete Research* 6, 773–782.
- Hofstetter, G. and H. Mang (1995). *Computational Mechanics of Reinforced and Prestressed Concrete Structures*. Braunschweig, Wiesbaden: Vieweg.
- Huber, H. (1991). Untersuchungen zum Verformungsverhalten von jungem Spritzbeton im Tunnelbau. Master's thesis, University of Innsbruck, Innsbruck, Austria. In German.
- Lackner, R. (2000). *Adaptive finite element analysis of reinforced concrete plates and shells*, Volume 89 of *Dissertationen an der Technischen Universität Wien*. Vienna: Österreichischer Kunst- und Kulturverlag.
- Lackner, R., C. Hellmich, and H. Mang (2001). Material modelling of brittle failure and creep in the framework of chemoplasticity. *International Journal for Numerical Methods in Engineering*. Submitted for publication.
- Lackner, R., J. Macht, C. Hellmich, and H. Mang (2001). Hybrid analyses of segmented shotcrete tunnel linings in squeezing rock. *Journal of Structural Engineering (ASCE)*. Submitted for publication.
- Lackner, R. and H. Mang (2000). Material modelling and computational strategies in the analysis of concrete shells. In *CD-ROM Proceedings of the European Congress on Computational Methods in Applied Sciences and Engineering*, Barcelona, Spain.
- Lackner, R. and H. Mang (2001). Chemoplastic material model for the simulation of early-age cracking: from experiments to the constitutive law. In A. Bentur (Ed.), *RILEM Int. Conf. on Early Age Cracking of Cementitious Systems*, Haifa, Israel.
- Lechner, M., C. Hellmich, and H. Mang (2001). Short-term creep of shotcrete - thermochemoplastic material modelling and nonlinear analysis of a laboratory test and of a NATM excavation by the finite element method. In P. Vermeer, S. Diebels, W. Ehlers, H. Herrmann, S. Luding, and E. Ramm (Eds.), *Continuous and discontinuous modelling of cohesive-frictional materials, Lecture notes in Physics*, Volume 568, pp. 47–62. Springer, Berlin.
- Mindess, S., J. Young, and F.-J. Lawrence (1978). Creep and drying shrinkage of calcium silicate pastes. I: specimen preparation and mechanical properties. *Cement and Concrete Research* 8, 591–600.
- Rokahr, R. and R. Zachow (1997). Ein neues Verfahren zur täglichen Kontrolle der Auslastung einer Spritzbetonschale. *Felsbau* 15(6), 430–434. In German.
- Ruetz, W. (1966). Das Kriechen des Zementsteins im Beton und seine Beeinflussung durch gleichzeitiges Schwinden. *Deutscher Ausschuss für Stahlbeton Heft* 183. In German.
- Sercombe, J., C. Hellmich, F.-J. Ulm, and H. A. Mang (2000). Modeling of early-age creep of shotcrete. I: model and model parameters. *Journal of Engineering Mechanics (ASCE)* 126(3), 284–291.
- Ulm, F.-J. (1998). Couplages thermochemomécaniques dans les bétons : un premier bilan. [Thermochemomechanical couplings in concretes : a first review]. Technical report, Laboratoires des Ponts et Chaussées, Paris, France. In French.
- Wittmann, F. (1982). *Creep and shrinkage mechanisms*, Chapter 6, pp. 129–161. Wiley, Chichester.
- Zachow, R. (1995). Dimensionierung zweischaliger Tunnel in Fels auf der Grundlage von *in-situ* Messungen. Technical Report 16, University of Hannover, Hannover. In German.